Controlling spatiotemporal pattern formation in a concentration gradient with a synthetic toggle switch

Içvara Barbier[1], Rubén Perez Carrasco[2*] and Yolanda Schaerli[1*]

[1] Department of Fundamental Microbiology, University of Lausanne, Biophore Building, 1015 Lausanne, Switzerland

[2] Department of Mathematics, University College London, Gower Street, WC1E 6BT London, United Kingdom

*Correspondence: r.carrasco@ucl.ac.uk and yolanda.schaerli@unil.ch

Abstract

The formation of spatiotemporal patterns of gene expression is frequently guided by gradients of diffusible signaling molecules. The toggle switch subnetwork, composed of two cross-repressing transcription factors, is a common component of gene regulatory networks in charge of patterning, converting the continuous information provided by the gradient into discrete abutting stripes of gene expression. We present a synthetic biology framework to understand and characterize the spatiotemporal patterning properties of the toggle switch. To this end, we built a synthetic toggle switch controllable by diffusible molecules in *Escherichia coli*. We analyzed the patterning capabilities of the circuit by combining quantitative measurements with a mathematical reconstruction of the underlying dynamical system. The toggle switch can produce robust patterns with sharp boundaries, governed by bistability and hysteresis. We further demonstrate how the hysteresis, position, timing, and precision of the boundary can be controlled, highlighting the dynamical flexibility of the circuit.

Keywords: Synthetic biology, gene regulatory networks, pattern formation, dynamical systems, bistability, hysteresis

Introduction

Synthetic biology aims to engineer living organisms with standardized and modular circuits that perform their functions in a programmable and predictable way (Brophy and Voigt, 2014, Cameron et al., 2014, Purcell and Lu, 2014). In addition to the promise of providing new technologies for medical and industrial applications (Gilbert and Ellis, 2018, Kitada et al., 2018, Nielsen and Keasling, 2016, Xie and Fussenegger, 2018), recapitulating biological processes synthetically provides a route to understanding the basic necessary mechanisms underpinning biological functions and dissect their properties and limitations (Bashor and Collins, 2018, Li et al., 2018).

Formation of spatiotemporal patterns of gene expression, a crucial process during the development of multicellular organisms, lends itself to be studied by such a synthetic biology approach. During development, pattern formation is achieved through a set of inter-connected gene regulatory programs encoding different non-linear responses to spatial chemical cues. This multiscale complexity makes the elucidation of the core principles of spatial patterning very challenging in living embryos, calling for alternative approaches capable of interrogating and comparing different pattern formation mechanisms. The rise of synthetic biology has successfully allowed to build synthetic systems able to explore core patterning principles (reviewed in (Santos-Moreno and Schaerli, 2019b, Luo et al., 2019, Davies, 2017, Ebrahimkhani and Ebisuya, 2019)). In addition, synthetic pattern formation is also an attractive technology for the engineering of living materials (Gilbert and Ellis, 2018, Nguyen et al., 2018, Moser et al., 2019, Cao et al., 2017) and tissues (Davies and Cachat, 2016, Healy and Deans, 2019, Webster et al., 2016).

One ubiquitous strategy of patterning during embryogenesis is positional information, in which signaling molecules – the morphogens – diffuse and generate concentration gradients to specify positions. Specific gene regulatory programs are able to translate the spatiotemporal information provided by the local concentration of morphogen gradients into robust gene expression patterns (Wolpert, 1996, Green and Sharpe, 2015, Rogers and Schier, 2011). This mechanism has been extensively used in synthetic systems to generate spatial patterns, especially stripe patterns, which were produced through synthetic feed-forward loops (Basu et al., 2005, Schaerli et al., 2014), inducible promoters (Grant et al., 2016) and AND-gates (Boehm et al., 2018).

One of the gene regulatory subnetworks able of interpreting positional information is the bistable genetic switch (Zhang et al., 2012, Srinivasan et al., 2014, Balaskas et al., 2012, Kraut and Levine, 1991, Lopes et al., 2008b, Perez-Carrasco et al., 2016, Sokolowski et al., 2012, Zagorski et al., 2017, Alon, 2007), known as toggle switch (TS) (Figure 1A). The topology of this circuit consists of two cross-repressing nodes that result in the binary mutually exclusive stable expression of one of the nodes. If the expression is influenced by an external signal, the TS provides a mechanism to convert a concentration gradient of this signal into stripes of gene expression (Perez-Carrasco et al., 2016, Sokolowski et al., 2012). Examples of TS-controlled pattern formation have been identified in the mesoderm formation in *Xenopus* (Saka and Smith, 2007), *Drosophila* blastoderm gap gene segmentation (Verd et al., 2019, Clark, 2017),

and neural specification in vertebrate neural tube (Briscoe and Small, 2015, Perez-Carrasco et al., 2018).

The non-linearity of gene regulatory networks such as the TS impedes to intuitively understand the effect that different kinetic parameters have on the dynamics of gene expression. For this reason, during the last decade, gene regulatory networks have been analyzed using tools from dynamical systems theory, associating the stable steady states of the dynamical system with the attainable gene expression states of a cell. Similarly, the change in the availability of cellular states as a consequence of perturbations of kinetic parameters of the network can be associated with the bifurcations of the dynamical system, providing information of the constraints of the possible cellular states. Indeed, the dynamical system of the TS has been thoroughly analyzed *in silico,* both in single cells as well as in population-level patterning scenarios (Perez-Carrasco et al., 2016, Ferrell, 2002, Guantes and Poyatos, 2008), showing that two possible stable states can coexist for a region of parameters inside which the expression state of the cell will depend on the initial gene expression – a phenomenon known as bistability. Under the control of an external signal, this bistability leads to hysteresis in which the state of the system is robust to signal changes, thus providing memory to gene expression patterns (Wang et al., 2009). Interestingly, the analysis of the steady states of the dynamical system not only provides static information of the cellular states, but also information on the transient dynamics of gene expression by which the states are attained (Verd et al., 2014). Therefore, a map of the underlying dynamical system is critical to fully understand the dynamics of the TS network.

The first synthetic version of the TS network was built almost 20 years ago and was a milestone of synthetic biology (Gardner et al., 2000). Since then, it has been built multiple times, extensively studied and used for its memory, bistability or hysteresis properties (Padirac et al., 2012, Purcell and Lu, 2014, Chen and Arkin, 2012, Lou et al., 2010, Andrews et al., 2018, Yang et al., 2019, Nikolaev and Sontag, 2016, Zhao et al., 2015, Sokolowski et al., 2012, Lebar et al., 2014), for stochasticity fate choice (Axelrod et al., 2015, Perez-Carrasco et al., 2016, Sekine et al., 2011, Wu et al., 2013, Lugagne et al., 2017) and to tune threshold activation (Gao et al., 2018). Nevertheless, its patterning capabilities controlled with a morphogen-like signal have not been studied in a synthetic system. Here, we constructed a “morphogen”-inducible synthetic TS network and studied its ability to produce spatial patterns - governed by bistability and hysteresis - in an *Escherichia coli* (*E. coli)* population. A combination of experiments and mathematical modelling allowed us to characterize the underlying bifurcation diagram, unveiling the possible dynamical regimes of the circuit. This enabled us to demonstrate how the inducible TS allows to control hysteresis, precision, position and timing of the pattern boundary.

Results

Inducible toggle switch topology and its spatial patterning behavior.

The inducible TS network consists of two mutually repressing nodes (Figure 1A). This mutual inhibition architecture ensures that only one of the nodes can be maintained at high expression. The dichotomous response of the cell depends on the asymmetry of the repression strengths and on the production rates of each node. An array of cells under a concentration gradient in charge of controlling any of these two properties will generate a binary spatial pattern. We built a synthetic inducible TS circuit starting from a characterized TS (Litcofsky et al., 2012). The first node of the network is composed of the TetR repressor and the mCherry reporter and will be referred hereon as the red node. The second node contains the LacI repressor and GFP reporter and will be referred as green node (Figure 1B). Accordingly, the two expression states that the circuit can maintain will be referred as green and red states. TetR and mCherry are regulated by the hybrid pLuxLac promoter (BBa_I751502), which is activated by the LuxR-AHL (N-(β-Ketocaproyl)-L-homoserine lactone) complex and repressed by LacI, whose repression strength can be regulated by isopropyl β-d-1-thiogalactopyranoside (IPTG). LacI and GFP are controlled by the pLtetO promoter, which is repressed by TetR. LuxR is constitutively expressed from a pLuxL promoter on a second plasmid (Figure 1B). In the absence of AHL (inducer), TetR and mCherry are not expressed, but LacI and GFP are, resulting in the green state. In the presence of AHL, TetR and mCherry can be expressed and repress LacI and GFP expression. Consequently, the system switches to the red state, provided that the concentration of the regulator (IPTG) is high enough.

We studied the capability of the inducible TS circuit to pattern an *E. coli* population exposed to different concentrations of AHL and IPTG and combinations thereof (Figure 1C-D). To this end, we grew the cells on a hydrophobic grid placed on an agar plate to give a defined spatial organization to the cells (Grant et al., 2016), while small molecules can freely diffuse between grid squares. AHL and IPTG were pipetted at the left and at the top edges of the grid, respectively, forming gradients of AHL and IPTG by diffusion. We then measured the bacterial fluorescence after overnight incubation. When the starting cells were in the green state (reached by previous incubation in the absence of AHL and IPTG), the switch to the red state was observed only in presence of both AHL and IPTG, in the top left corner of the grid (Figure 1C). In contrast, the same experiment performed with cells initially in the red state (reached by previous incubation in the presence of AHL and IPTG), showed that the red state is maintained above a certain concentration of AHL, mostly independent of the concentration of IPTG, leading to a green domain at the right (Figure 1D). An overlay of the two grid patterns allows to highlight the possible stable states available for different concentrations of AHL and IPTG showing two monostable regions for the red and green states, and a bistable region for low values of AHL and high values of IPTG that grant hysteresis to the system (Figure 1E). In addition to the tuning of the LacI repression by IPTG as explored here, the TetR repressing strength can be regulated by the addition of anhydrotetracycline (aTc) (Supplementary Figure 1A). Different combinations of gradients of AHL, IPTG and aTc result in different patterns (Supplementary Figure 1B-D), revealing the flexibility of the TS to control spatial gene expression.

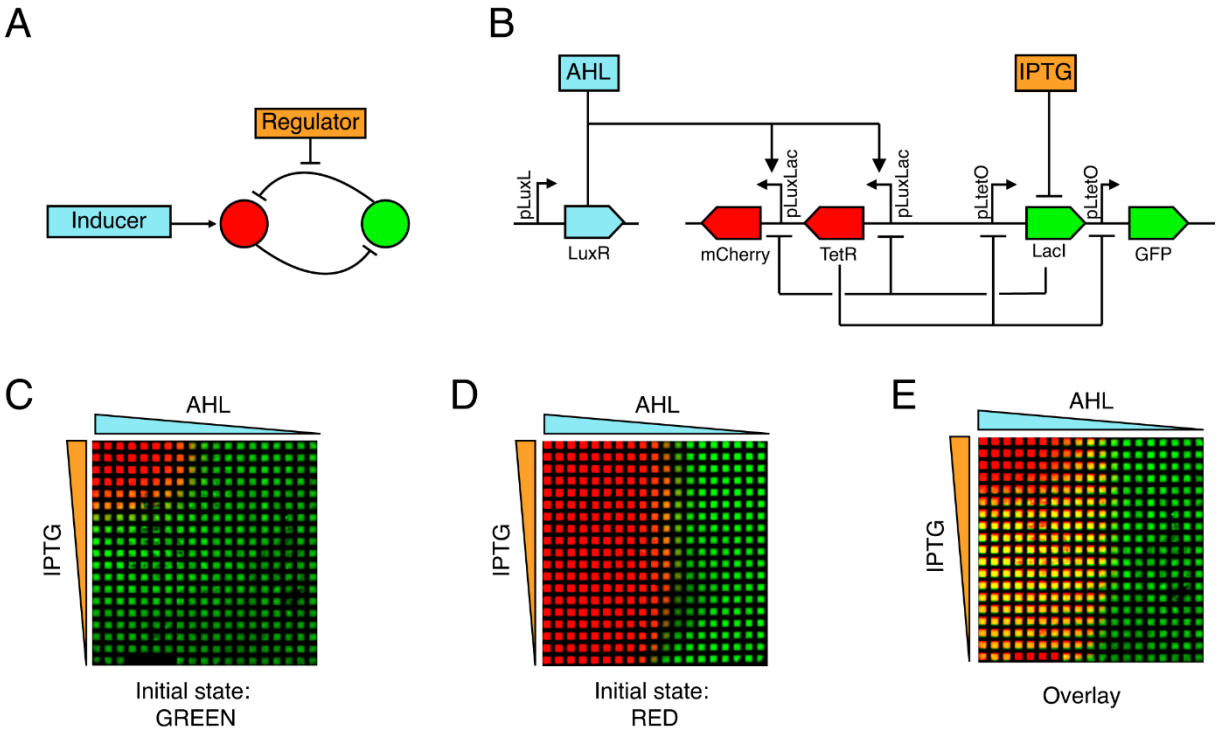

Figure 1: Inducible toggle switch topology and its spatial patterning behavior.

A. Schematic of the inducible toggle switch network composed of two mutually inhibitory nodes. The expression of the red node is controlled by an inducer, while a regulatory molecule can be added to tune the repression strength of the green node. **B.** Detailed representation of the molecular implementation of the network in (A) using SBOL annotation (Beal et al., 2019). **C-D**. 2D spatial patterning of a population of *E. coli* cells harboring the inducible toggle switch network. The colors correspond to the levels of fluorescence of mCherry (red) or GFP (green) produced by bacteria grown on a grid. 5 µl of aqueous solutions of 100 mM IPTG and 100 µM AHL were added at the grid edges forming gradients by diffusion as indicated by the triangle shapes. Before growing on the grid, bacteria were turned into the green (C) or red state (D) as indicated at the bottom. The grids were imaged after overnight incubation. Each grid square measures 0.75 x 0.75 mm^2. **E.** Overlay of the grids of C and D, highlighting the hysteresis of the system in yellow, resulting from the superposition of red and green fluorescence.

Characterization of the toggle switch as a dynamical system

To quantitatively analyze the network behavior with single cell resolution, we grew the TS bacteria in liquid culture for 10 h with defined concentrations of inducer (AHL) and regulator (IPTG) molecules and used flow cytometry to measure the green and red fluorescence of individual bacteria (Figure 2A). We gated the bacteria to quantify the percentage of cells in the red or green state for different inducer and regulator concentrations and different initial states. The observed behavior is consistent with the spatial patterning on the grid: Starting with an initial population of bacteria in the green state, the entire population (>90% of events) switched to the red state at high concentrations of both AHL and IPTG, whereas they stayed green otherwise. On the other hand, starting in the red state, the entire population stayed red above AHL concentrations of ~11 nM, but switched to the green state at lower AHL concentrations.

At the boundary between the red and green areas (white squares in Figure 2A), we observed cells in both flow cytometry gates. At high IPTG concentrations (≥0.5mM), a single population was located at intermediate red and green fluorescence values, whereas at IPTG concentrations ≤0.5mM the population split into two subpopulations displaying either the red or the green state. A bimodal distribution at the boundary between the two stable states is a known phenomenon of bistable circuits (Axelrod et al., 2015, Wu et al., 2013, Sekine et al., 2011) and can be caused by cell state switching in response to intrinsic gene expression noise (Perez-Carrasco et al., 2016, Sekine et al., 2011).

The transition from red to green is less affected by the concentrations of IPTG than the transition from green to red, because of the asymmetry of the network. In the transition from red to green, the rate-limiting step is the degradation and dilution of TetR in the cells, since the clearance of TetR is required before changes in AHL or IPTG concentrations can induce the switch. Therefore, for the rest of the manuscript, we will focus on initial green state populations, while the data for the initial red state is in the supplementary data (Supplementary Figures 4 and 5).

In order to fully characterize the dynamical capabilities of the circuit, we described the network with a mathematical model composed of ordinary differential equations (ODE) capturing the concentration of all the chemical species over time (see Methods for details). To unveil the dynamical landscape compatible with the synthetic circuit, we parameterized the model by fitting it to our experimental data. In order to do so, we made use of multitry Markov chain Monte Carlo (MCMC) inference (Laloy and Vrugt, 2012, Shockley et al., 2018), with a likelihood function based on the experimentally measured levels of expression and number of steady states found for the different concentrations of AHL and IPTG tested. We obtained a narrow probability distribution for all 11 parameters (Supplementary Figure 2). The predicted outputs from the parametrized equation were able to recapitulate the bistability and hysteresis observed in the experimental data (Figure 2B and Supplementary Figure 3). This allowed us to reconstruct the multidimensional bifurcation diagram of the system (Figure 2C) which we can use as a map to predict the effect that different dynamical gradients will have on the observed gene expression patterns.

Analysis of the bifurcations of the system shows a scenario compatible with other TS, in which a continuous variation of AHL or IPTG can change the number of stable states via saddle-node bifurcations. Starting from a bistable condition, a saddle-node bifurcation occurs through the collision of a stable and an unstable state of the system, leaving only one possible stable state left (Figure 2C). For a cell in the state about to disappear, a small perturbation of IPTG or AHL induces a sharp switch to the opposite state, producing a sharp transition between cell states.

There are two different saddle-node lines in the phase plane (AHL, IPTG) of the bifurcation diagram that collide at a certain concentration of the inducers (around 10^{-3} μM AHL and 10 mM IPTG). Called a cusp bifurcation, this point separates the regions of inducer in the phase plane in which the switch between states occur through a saddle-node bifurcation (bistability) or through the continuous change of

expression of a monostable state. Thus, the availability of a cusp point allows to explore the properties of two different patterning strategies (bistability versus sigmoidal response) for the same circuit topology.

Controlling the hysteresis, position, and sharpness of the boundary

Next, we analyzed how the IPTG concentration influences the hysteresis of the circuit, characterized by the range of inducer concentrations for which the circuit shows bistability (Figure 2D). Since IPTG is in control of the repression of the green node over the red node, it is a perfect candidate to control the hysteresis of the TS. Based on the bifurcation diagram, we expected that the lower the IPTG concentration (i.e. the stronger the repression on the red node), the bigger the range of bistability. Testing the bistability of the circuit at different IPTG concentrations confirmed this hypothesis, showing a response without bistability to an AHL gradient at high values of IPTG (10 mM) and an increasing range of bistability as IPTG decreases. The highest amount of hysteresis is observed in the absence of IPTG. Here, cells are not able to switch from green to red, even in presence of high AHL. However, AHL is enough to preserve the red state once reached. We thus observed three different dynamic regimes with distinct ranges of hysteresis: 1) no hysteresis (>1 mM IPTG) in a sigmoidal regime. 2) hysteresis, in a bistable regime with the possibility to switch between both states (around 0.125 mM IPTG) and 3) hysteresis in a bistable regime with irreversibility of the green state (around 0 mM IPTG). Those three regimes were also observed as spatial patterns on the grid, when placed on agar plates with uniform IPTG concentrations (Figure 2D, right).

In addition to controlling the transition between a sigmoidal and a bistable regime and consequently the hysteresis, the IPTG concentration also affects the position of the boundary between the red and green states. Higher concentrations of IPTG allow the system to switch from green to red at lower AHL concentrations (Figure 2A and D), thus controlling the boundary position for a given AHL gradient. Finally, IPTG also tunes the transition sharpness between the red and green states (Figure 2E and Supplementary Figure 4). Starting from the green state, at high concentrations of IPTG beyond the cusp point, we observed a sigmoidal expression response in an AHL concentration gradient, similar to the one expected from a circuit with a single repressor (TetR) active. At lower IPTG concentrations, below the cusp point, the system displayed a sharper transition as expected from the saddle-node bifurcation. Moreover, these different transitions are consistent with the distinct population behaviors during cell state transitions along the gradient: a smooth transition of a single population for the sigmoidal behavior and a bimodal population transition (Figure 2A) for the bistable switch behavior. In summary, the regulator IPTG allows us to choose between a bistable and a sigmoidal regime (at high IPTG concentrations) and thus to control the hysteresis, the position and the sharpness of the boundary.

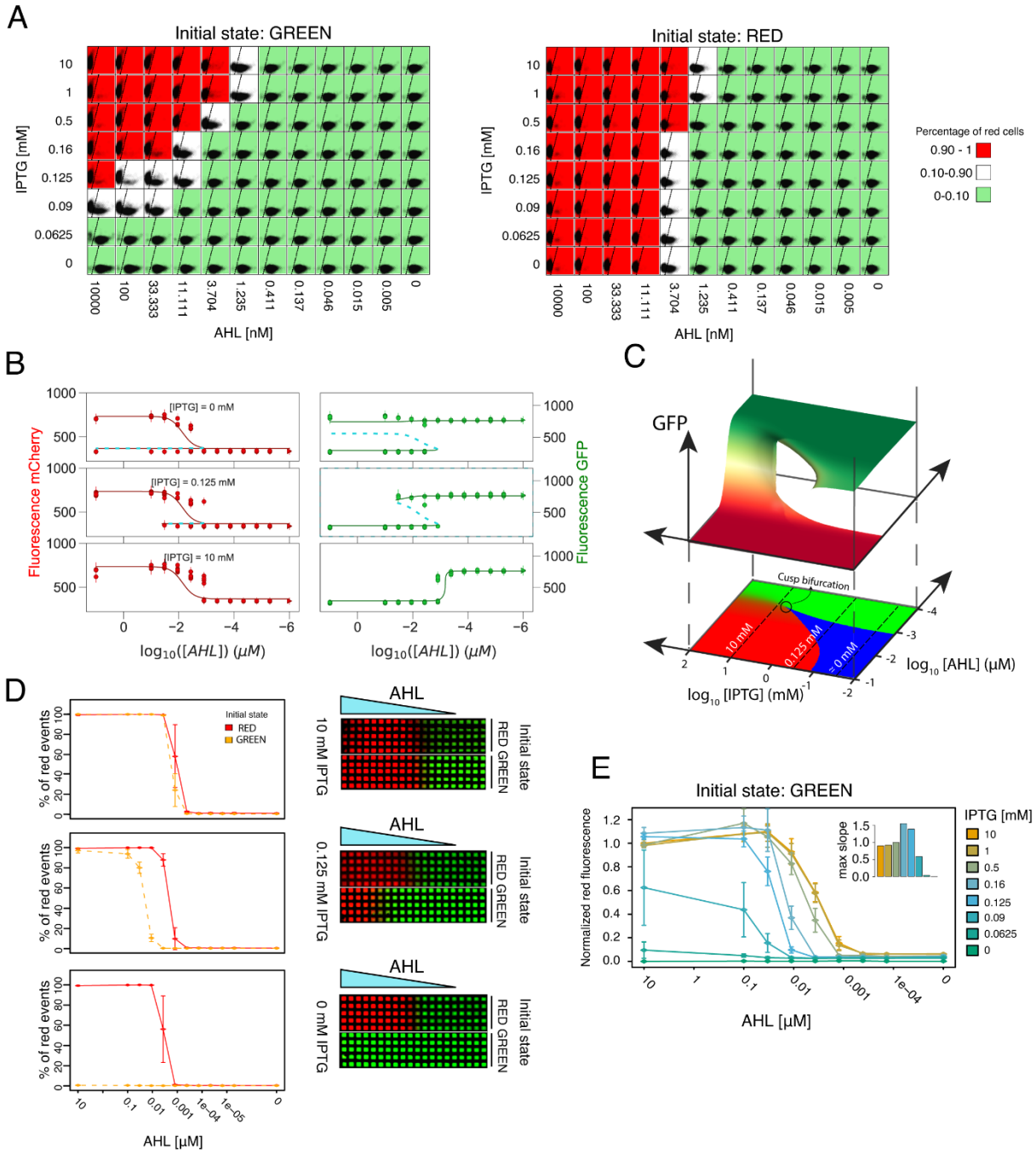

Figure 2: Controlling the hysteresis, position, and sharpness of the boundary.

A. Quantitative single cell analysis of the inducible toggle switch. Overview of the flow cytometry data of a representative replicate. Each square shows red (Y-axis) and green (X-axis) fluorescence of the population (10'000 events) measured at indicated concentrations of IPTG and AHL after 10 h of incubation. Background color corresponds to the percentage of red gated events as indicated. **B.** Comparison between the observed populated states from the flow cytometry data (circles) and the available steady states predicted by the model (solid lines: stable states, dashed lines: unstable states), shown for 3 IPTG concentrations. The median and the standard deviation of the experimentally observed states of the gated populations are shown. Parameters used in the model are the best parameter candidates from the MCMC fitting (Table 1). The whole data set is shown in Supplementary Figure 3. **C.** Top: Bifurcation diagram for the parameters found in the fitting, showing the stable steady states available for different combinations of [AHL] and [IPTG]. Bottom: Phase portrait of the TS, indicating monostable regions in red/green proportionally to the concentrations of mCherry/GFP and bistable conditions in blue. The circle indicates the cusp bifurcation. **D.** Hysteresis at three different IPTG concentrations, corresponding to the three different regimes showed in (C) as

dashed lines. Left) Mean percentage of red cells for different concentrations of AHL are shown for an initial population in the red state (solid red lines) and for an initial population in the green state (dashed orange lines). Error bars show standard deviation of 3 biological replicates. Right) Grid patterns at constant IPTG concentrations. 5 µl of a solution of 100 µM AHL were added at the left to create the gradient. Colors correspond to the intensity of red and green fluorescence. **E.** Sharpness of the boundary. Normalized red fluorescence for an initial population in the green state in an AHL gradient at different IPTG concentrations. Mean and standard deviation of 3 biological replicates. The inset bar plots represent the maximum slope of each curve (Supplementary Figure 3).

Temporal dynamics of the patterning

So far, we investigated the influence of IPTG on the pattern in an AHL gradient by studying the static spatial gene expression after overnight incubation. However, in order to understand the process of pattern formation it is of paramount importance to study the temporal dynamics of the patterning process. To this end, we measured the fluorescence of the cells at different concentrations of IPTG and AHL over a time course of 10 h with flow cytometry (Figure 3, Supplementary Movie 1, Supplementary Figure 5). We observed that gradients inducing a pattern across a bistable region have a slower and position-dependent response than those patterning across a sigmoidal region. In particular, the time to switch from green to red (>90% red events) depends on the concentration of IPTG, switching at 4 h at high IPTG concentrations (10 to 0.5 mM) and after 6 h and 8 h for lower IPTG concentrations (0.16 and 0.125 mM, respectively) (Figure 3A). Similarly, for a constant amount of IPTG, the switching time depends on the AHL concentration, switching at times as slow as 6-10 hours for an IPTG concentration corresponding to the bistable region (0.125 mM Figure 3B). On the other hand, inducing a pattern in the sigmoidal regime (10 mM IPTG), we observe a more consistent switching time (4 h) across different AHL concentrations (Figure 3C).

Interestingly, the behaviors of the switch at the population level over time are identical to the ones observed across different AHL concentrations: at high IPTG (beyond the cusp bifurcation, in the sigmoidal regime) we measured one population moving as a whole, while at lower IPTG concentrations (bistable regime) we observed the cells splitting into two divergent subpopulations (Figure 3A,B and Supplementary Movie 1), suggesting that the dynamics of the sigmoidal patterning are a result of the population relaxing to the unique possible steady state, whereas in the bistable regime the transition is controlled through the stochastic switching between the two possible states, with a time that is determined by the intrinsic noise and can therefore be slower than the degradation rate of the proteins composing the TS.

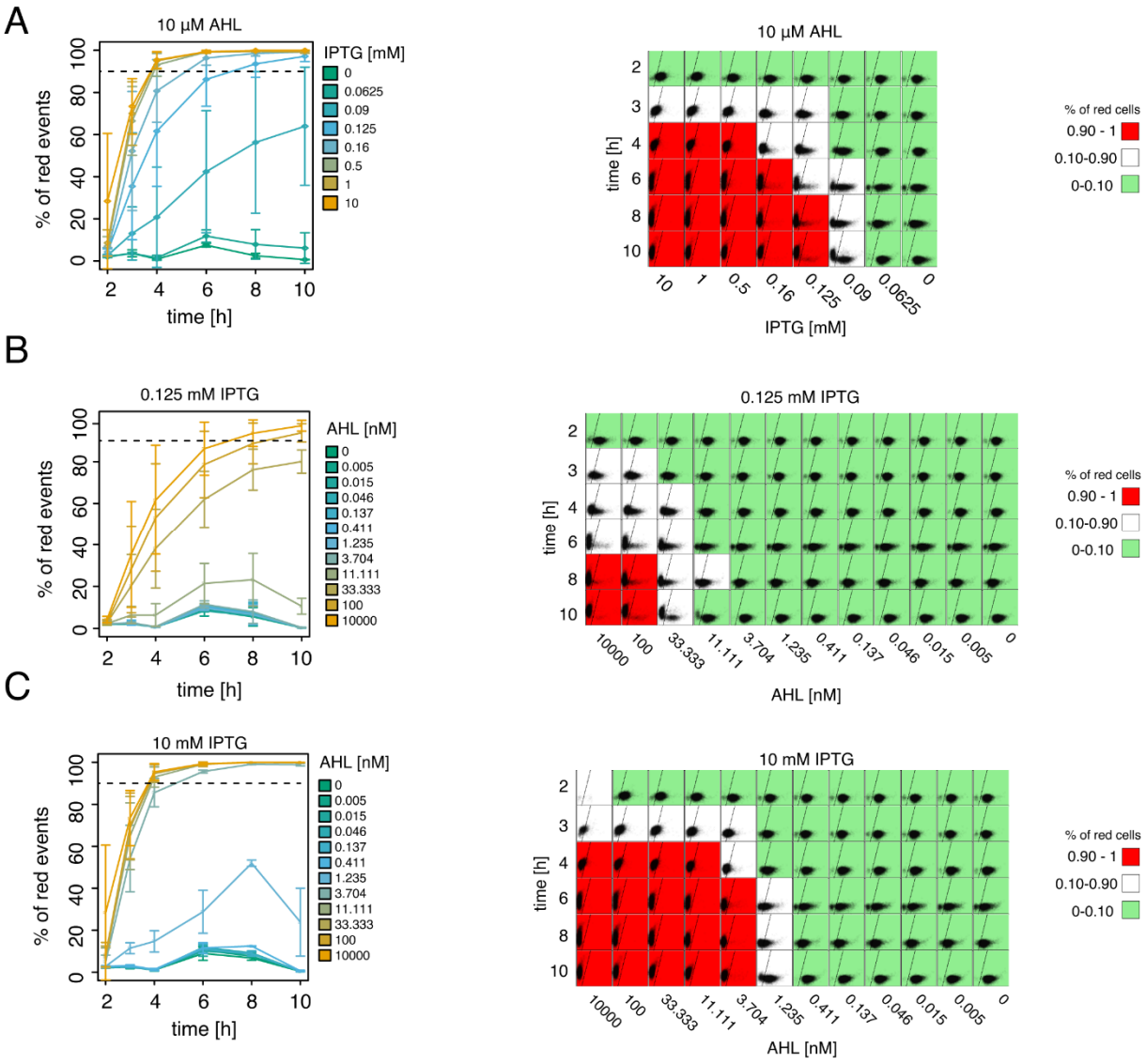

Figure 3: Temporal dynamics of patterning with the inducible toggle switch.

A-C. Effects of IPTG and AHL concentrations on the switching time from the green to the red state. For plots in the right column, each square represents flow cytometer data of 10,000 events measuring red (Y-axis) and green fluorescence (X-axis). Background color of each square indicates if >90% of the events are in the red or the green gate. Plots in the left column show the percentage of cells in the red gate over time. Points indicate the mean and standard deviation of 3 biological replicates. Dashed lines indicate the 90% threshold used to color the flow cytometry plots. **A.** Analysis of state transition over time in the presence of different IPTG concentrations and a high level of AHL (10 µM). **B-C.** Analysis of state transition over time in the presence of different AHL concentrations and two different IPTG concentrations corresponding to the sigmoidal (10 mM) and bistable regimes (0.125 mM).

Patterning in the sigmoidal regime is faster than in the bistable regime

Combining our model with 2D diffusion allowed us to reproduce the patterns observed in the grid assay shown in Figure 1 (Figure 4A). In addition, integrating the diffusion of the inducer with the dynamical properties of the bifurcations of the system can shed light on the different patterning dynamics observed. In particular, consistent with our flow cytometry data (Figure 3), the model suggests that the switching slows down close to the saddle node bifurcation, a phenomenon called critical slow down. Thus, for different constant values of IPTG, a gradient of AHL is expected to create a moving boundary at different

speeds for cells switching from the green to the red state (Figure 4B) (Perez-Carrasco et al., 2016). To test this prediction, we measured the position of the boundary over time in the grid assay at two different IPTG concentrations corresponding to two different dynamical regimes (sigmoidal, 1 mM and bistable, 0.125 mM) (Figure 4B). As expected, we observed that the transition to the production of mCherry starts earlier and advances faster in the sigmoidal regime, equipping the TS with time control of the pattern formation through the cusp bifurcation. This was confirmed through simulation of the diffusion of the inducers on the grid, were the model predicts the same trend than the experimental data, with no more than three squares of difference. On the other hand, we did not observe clear differences in the precision of the boundary in the grid assay, probably due to a lack of precision in the concentration gradients accessible by the grid.

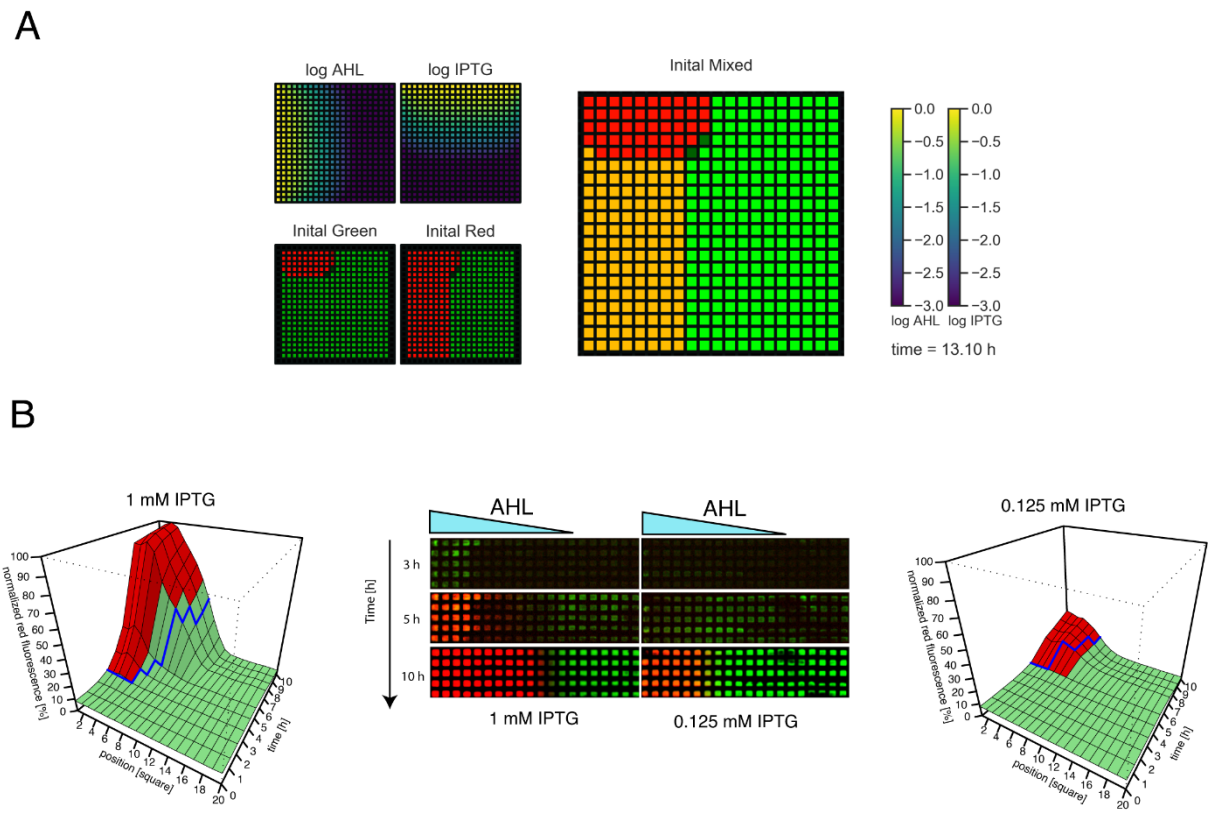

Figure 4: Patterning in the sigmoidal regime is faster than in the bistable regime

A. Modelling of the pattern observed in the grid assay (Figure 1C-E). Top left: AHL diffusion from left to right and IPTG diffusion from top to bottom. Bottom left and right: Colors represent the state of the system, green for GFP/LacI expression, red for mCherry/TetR expression, and yellow when both states are possible depending on the initial state. **B.** Time course of pattern formation in the grid in the sigmoidal (1 mM IPTG, left) and bistable (0.125 mM, right) regimes. Center: Before growing on the grid, bacteria were turned into the green state. The indicated concentration of IPTG was homogeneously present in the agar plate and 5 µl of 100 µM AHL were loaded at the left edge of the grid. The grids were incubated at 37° C and imaged at the indicated times. A representative replicate is shown. Left and right 3D plots represent the quantitative analysis of mean red fluorescence intensity in the grid over time and position of 3 biological replicates. Blue lines represent the boundary predictions from the mathematical model. Green and red colors correspond to measurements where the red fluorescence intensity is below or above 50% of the highest intensity measured along the AHL gradient at each timepoint, respectively, corresponding to how the boundary was defined *in silico* (see Methods for details).

Spatiotemporal control of the pattern by using spatially homogenous signals

In addition to the pattern formation through a bistable or monostable sigmoidal regime, the TS offers the possibility to move between both different regimes during the pattern formation, allowing for different patterning strategies that can exploit the properties of both regimes. In particular, by manipulating the homogeneous levels of IPTG in time for a given gradient of AHL, we can control the pattern formation process. An initial population of cells in the green state in the absence of IPTG (bistable irreversible regime) is unaffected by the gradient of AHL. Adding IPTG homogeneously at the desired time point, brings the cells to the sigmoidal monostable regime able to respond to the gradient of AHL and forming a boundary. Once the boundary is located at the desired position, removing IPTG takes the system back to the bistable zone, thus freezing the boundary and making it robust to changes in AHL (Figure 5A). Consequently, the system is able to maintain a pattern in the absence of IPTG which removes the requirement of maintaining a precise AHL gradient to keep the pattern boundary. Therefore, a pulse of IPTG can combine advantages of two distinct regimes: of the sigmoidal monostable regime for a fast establishment of a pattern (Figure 4) and of the irreversible regime to make the pattern robust to changes in the AHL gradient. To demonstrate this effect, we grew cells initially in the green state at different concentrations of AHL and exposed them to pulses (2 h, 3.5 h ,5 h, 6.5 h) of 10 mM IPTG (Figure 5B). We then grew them for further 6 h in the absence of IPTG, but keeping the AHL concentrations used during the pulse. Indeed, cells receiving enough AHL (>= 0.01 µM), were able to maintain the red state. Interestingly, this was the case even for short pulses were not the whole population did have enough time to switch (2 h). For intermediate values of AHL, close to the boundary, the final state of the population depends on the position of the population with respect to the basins of attraction of the bistable regime. In particular, it is noteworthy that if the single cell population at the end of the pulse is located at intermediate green and red fluorescence levels, it splits into two subpopulations (green or red fluorescence) when brought back to the bistable regime.

We used the grid assay to further demonstrate this memory property of the TS and to show that the pattern in the bistable regime is indeed robust to changes in the AHL gradient. We patterned a grid as in Figure 1 and transferred the cells onto a new agar plate where the positional information provided by AHL and IPTG was removed (0 mM IPTG, homogeneous concentration of 5 µM AHL). As predicted, the pattern was maintained in the absence of any spatial information (Supplementary Figure 6). This result demonstrates that an inducible TS network is capable of interpreting spatiotemporal gradients by making use of the memory properties of the circuit.

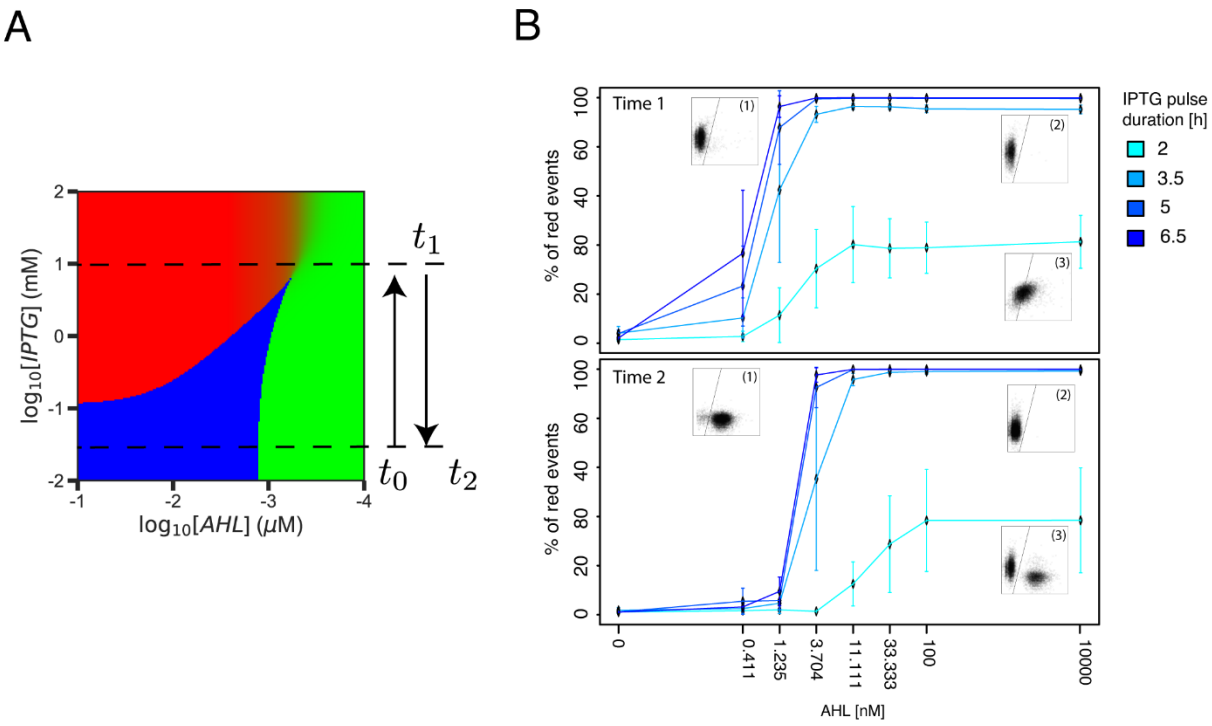

Figure 5: A homogeneous pulse of IPTG allows to control the pattern formation. A. Schematic of the protocol used. Cells initially in the green state for low levels of IPTG (irreversible bistable regime) are exposed to a pulse of high IPTG (at time t_0) bringing the system to the sigmoidal region where a gradient of AHL can induce a pattern. Removing IPTG (at time t_1) takes the system back to the bistable zone, thus freezing the boundary and making it robust to changes in AHL (at any posterior time t_2). **B.** Response of the system to IPTG pulses of different durations (2- 6.5 h) at different AHL concentrations. Cells were grown in the presence of 10 mM IPTG and the indicated amount of AHL and analyzed by flow cytometry. The top graph displays the percentages of red cells observed just after the incubation with IPTG (time 1, t_1). Next, the cells were diluted and grown for another 6 h without IPTG, but with the same concentration of AHL as during the IPTG pulse. The bottom graph displays the percentage of red cells observed after this incubation ($\text{time } 2, t_2$). Inset graphs represent red (y-axis) and green (x-axis) fluorescence measured by flow cytometry (10,000 events). The following conditions are shown: (1) 6.5 h pulse, 1.235 nM AHL. (2) 6.5 h pulse, 10000 nM AHL. (3) 2 h pulse, 10000 nM AHL.

Discussion

Systems displaying hysteresis, and in particular the bistable switch, allow for a sharp threshold response that can turn a graded input into a binary output (Perez-Carrasco et al., 2016, Sokolowski et al., 2012). Interestingly, the mutual repressing motif of the toggle switch is widely found in natural pattern-forming systems, for example, in networks responsible for patterning the neural tube (Balaskas et al., 2012), the dorsal telencephalon (Srinivasan et al., 2014), the *Drosophila* embryo segments (Verd et al., 2019, Clark, 2017) and the *Xenopus* mesoderm (Saka and Smith, 2007). However, in addition to forming sharp boundaries, the successful formation of a pattern requires the control of the position and timing of the boundary formation. In order to explore dynamic patterning properties of the TS gene regulatory network, we have successfully built and characterized a synthetic inducible toggle switch with tunable repression (Figure 1).

We quantified the gene expression at the single cell level over a wide range of inducer and regulator concentrations and fit the data to parameterize a mathematical model of gene regulation. The resulting

bifurcation diagram of the dynamical system provided the mechanistic understanding required to interpret the different spatiotemporal patterns observed and experimental design guidance for pattern formation with the synthetic TS. In particular, this approach allowed us to characterize the mechanism by which the system can transit from a bistable regime to a sigmoidal unimodal response to the inducer, determined by the cusp bifurcation of the dynamical system (Figure 2). From the exploration of the differences in boundary precision of both regimes, we observed that while the bistable regime provides the sharper boundary (as previously reported (Lopes et al., 2008a, Isalan et al., 2005)), the sigmoidal regime allows for a faster response (Figures 3 and 4). This reveals a trade-off between the timing and precision of the boundary. These observations are in consonance with dynamical systems predictions, in which the sharp transition of the bistable regime - through a saddle-node bifurcation - comes at the price of the critical slowing down close to the bifurcation (Narula et al., 2013, Perez-Carrasco et al., 2016).

In addition, for different levels of a spatially homogeneous regulator, we have been able to control the range of hysteresis and the position of the pattern boundary for a given inducer gradient changed accordingly (Figure 2). This mechanism is analogue to the one proposed by Cohen *et al*. (Cohen et al., 2014) to control the boundary position of patterns regulated by morphogen gradients by changing the affinity of one of the elements to a spatially homogeneous transcription factor. This result highlights the evolutionary potential of the circuit, allowing for kinetic mechanisms of controlling the position of the boundary without compromising other aspects of the boundary or requiring an upstream regulation of the morphogen gradient.

Further to controlling the position of the pattern, the range of bistability can also lead to an irreversible switch for a wide range of the parameter space. Inside this region of the parameter space, any prepattern can be robustly fixed, only requiring the morphogen information for a certain time window (Figure 5, Supplementary Figure 6). Coupled with the dynamics of boundary formation, this provides alternative patterning strategies to the classical static positional information, in which the precision, position and timing of the boundary can be controlled by the dynamic properties of the upstream signal. This flexibility is of utmost importance in developmental scenarios, where both, the morphogen signalling and the patterns are dynamic processes during tissue differentiation, such as the boundary position movement during the gap gene segmentantion in *Drosophila* (DiFrisco and Jaeger, 2019), or the adaption of the signalling of sonic hedgehog morphogen during neural differentiation in the patterning of the neural tube (Balaskas et al., 2012). In this latter scenario, the adapatation to the gradient of sonic hedgehog (through Gli signalling) results in a combination of temporal profiles of activation and repression acting on the patterning circuit (Junker et al., 2014, Cohen et al., 2015). This highlights the importance to understand bistable switches inside a dynamical scenario. While such dynamics is challenging to measure in the developing embryo, our synthetic biology framework allowed for an alternative route towards understanding the dynamics of the TS in pattern formation.

Our improved understanding of the TS for pattern formation opens up new avenues of research. In particular, for many bistable parameter conditions, single cell expression showed the coexistence of two subpopulation of cells at each one of the available stable states. This provides evidence of the relevance of intrinsic noise in the establishment of the pattern. While previous *in silico* research shows that intrinsic noise can determine the position and precision of morphogen driven boundaries (Perez-Carrasco et al., 2016, Weber and Buceta, 2013), the actual role of noise in the dynamics of pattern formation in living systems and the possibility of optimal dynamical strategies based on the stochasticity of gene expression remain still a conundrum. In addition, it poses new challenges to dynamical system inference in which different sources of intrinsic noise must be disentangled from measurement noise in order to obtain an accurate characterization of the circuit (Dharmarajan et al., 2019).

Overall, our results underscore the relevance of studying the dynamical context of a gene regulatory network in order to understand patterning processes, not only of synthetic circuits but also of developmental systems (Ferrell, 2002, Sagner and Briscoe, 2017). Future work will reveal if the TS properties are conserved when incorporated in more complex (synthetic) gene regulatory networks, for example when combined with the repressilator (Elowitz and Leibler, 2000, Potvin-Trottier et al., 2016, Santos-Moreno and Schaerli, 2019a) to yield the AC-DC network (Perez-Carrasco et al., 2018, Verd et al., 2019, Balaskas et al., 2012, Panovska-Griffiths et al., 2013). Moreover, the here established engineering guidelines on how to control patterning with a synthetic TS will be valuable for future synthetic pattern formation, for example in the context of engineered living materials based on bacterial biofilms (Gilbert and Ellis, 2018, Nguyen et al., 2018, Moser et al., 2019, Cao et al., 2017).

Materials

Media

Cloning experiments used lysogeny broth medium (LB: 10g Bacto-tryptone, 5 g yeast extract, 10 g NaCl per 1 l) supplemented with the appropriate antibiotic (25 µg/ml kanamycin or 25 µg/ml spectinomycin). All experiments with the synthetic circuit were performed in M9 minimal medium (1x M9 salts, 2mM MgSO4, 0.2mM CaCl2, 0.0005% (w/v) thiamine) with 0.2% (w/v) glucose as carbon source, supplemented with 0.1% (w/v) casamino acids and the appropriate antibiotics (25 µg/mL kanamycin and 25 µg/ml spectinomycin)

Reagents

Restriction enzymes, alkaline phosphatase from calf intestine (CIP), DNA Polymerase I large (Klenow) fragment and T4 DNA ligase were purchased from New England BioLabs (NEB). Oligonucleotides and chemicals were obtained from Sigma-Aldrich. Polymerase chain reactions (PCRs) were carried out with Q5 Hot Start High-Fidelity DNA polymerase (NEB). Colony PCRs were performed with Taq polymerase (NEB). PCR products and digested plasmids were purified with the Monarch PCR & DNA Cleanup Kit (NEB). Plasmids were purified using the QIAprep Spin Miniprep Kit (QIAGEN).

Methods

Cloning of the inducible toggle switch circuit

We cloned the morphogen inducible toggle switch plasmid (“TS_pLuxLac”) from an already functional toggle switch plasmid (pKDL071) (Litcofsky et al., 2012), kindly provided by Jeong Wook Lee. The two Ptrc-2 promoters upstream of TetR and mCherry coding sequences were replaced by the hybrid promoter pLuxLac (BBa_I751502) with the plug-and-play method initially used to assemble pKDL071 using the restrictions sites NcoI and SalI upstream of TetR and XmaI and MfeI upstream of mCherry.
For the “pCDF_luxR” plasmid, the pLuxL promoter (BBa_R0063) and the LuxR gene (synthesized by GenScript) were introduced into a pCDF plasmid with a customized multiple cloning site (Schaerli et al., 2014) between the KpnI and BamHI sites. The sequences and plasmids will be available through Addgene.

Strain and growth condition

pCDF_luxR and TS_pLuxLac were transformed into the *E. coli* strain MK01 (Kogenaru and Tans, 2014). The absence of the *lacI* gene in this strain avoids unexpected cross talk between the synthetic circuit and the host.

Bacteria were turned into red state by inoculating single colonies into 4 ml M9 medium in presence of 1 mM IPTG (isopropyl β-D-1-thiogalactopyranoside) and 10 µM AHL (N-(β-Ketocaproyl)-L-homoserine lactone). They were grown overnight at 37° C and 200 RPM shaking. The same procedure was used to turn the bacteria into the green state, with the difference that the medium did not contain IPTG and AHL. These bacteria were plated out on LB agar plates (supplemented with 10 µM AHL for the red state) and

incubated overnight at 37° C. The plates were stored at 4° C and single colony from them were picked for the experiments.

Flow cytometry

Single colonies in the red or green state were cultured in M9 for 4-6 h and put at 4° C before entering in stationary phase (below 0.8 OD). The following day, these cultures were diluted to 0.01 OD (NanoDrop 2000, Thermofisher) and added into the wells of a 96-well plate (CytoOne) to a total volume of 120 µL including indicated concentrations of AHL and IPTG. The plate was incubated in a BioTek Synergy H1 plate reader at 37° C with 548 cpm (2 mm) double orbital shaking speed. Absorbance (600 nm) was monitored every 10 min to check that cells did not enter stationary phase (below 0.3 in the plate reader) as cells in stationary phase can no longer switch between the two states. After 5 h, cells were diluted 100 times before incubating them again under the same conditions for a total of 10 h.

At indicated times, 5 µL of the cell cultures were diluted into 95 µL of phosphate-buffered saline (PBS) and analyzed by flow cytometry (BD LSRFortessa™) with 488 nm excitation and FITC filter for measuring GFP fluorescence and 561 nm excitation and PE-Texas Red filter for measuring mCherry fluorescence. 10,000 events were recorded and analyzed by FlowJo and a custom-made R script.

First, cells were gated with FlowJo in the SSC-H and FSC-H scatter plot. Next, FITC-H and PE-Texas Red-H data were exported to be analyzed in R. The red and green gates were set with the help of positive controls for red and green fluorescence. These controls were an overnight culture of our bacteria in presence of 1 mM IPTG and 10 µM AHL for red and without any inducer for green. In the figures, percentages of red cells correspond to the percentages of cells found in the red gate and the red fluorescence mean corresponds to the mean of red fluorescence of all the gated cells normalized to the red fluorescence of the cells grown at the highest AHL and IPTG concentrations and corrected for the background fluorescence (minimal red fluorescence value measured in the experiment).

For the IPTG time pulse experiment, we started the experiment with a culture of OD 0.1 in a medium containing 10 mM IPTG and the indicated concentration of AHL. The samples were incubated as described above until the first time point (2 h) and an aliquot was stored at 4° C. Then, the cells were diluted 1:5 into fresh medium containing the same IPTG and AHL concentrations and further incubated until the next time point (3.5 h). This procedure was repeated for all time points. An aliquot of each sample was analyzed by flow cytometry once all samples were collected. The next day, the cells where diluted 1’000 times into fresh medium with the indicated concentration of AHL and no IPTG. The cells were grown for 6 h and directly measured by flow cytometry.

Grid assay

Single colonies in the red or green state were cultured in M9 for 4-6 h and put at 4° C before entering in stationary phase (below 0.8 OD). The following day, these cultures were washed from IPTG and AHL by centrifugation for 1 min at 13’000 RPM and resuspended in fresh medium without IPTG or AHL. Then cells were diluted to an OD of 0.1 before being pipetted onto the grid (ISO-GRID from NEOGEN) (Grant et al., 2016) (20 µl of cells were loaded for 10 lines, approximatively 0.05 µl per square) that was placed on a M9 agar plate with 0.2% (w/v) glucose and appropriate antibiotics (25 µg/mL kanamycin and 25

µg/mL spectinomycin). The inducers (100 mM IPTG and 100 µM AHL, 5 µl each) were added as indicated in the figures. The plate was incubated overnight at 37° C before green and red fluorescence were measured with a Fusion FX (VILBER) imaging system. We used 0.2 ms exposure with blue light (480nm) and a F-565 filter for the GFP measurement and 1 min exposure with red light (530nm) and F-740 filter for mCherry. ImageJ software (R Core Team, 2017) was used to analyze the picture.

For the time course experiment, bacterial solution with an OD of 3 were loaded on the grid in order to be able to quantify early timepoints. Fluorescence intensity values for each square of the grids were extracted with a custom Fiji imageJ (Schindelin et al., 2012) macro script and the maximum value for each square was normalized to the highest measured fluorescence in all the conditions and replicates. The data was plotted with R software (R Core Team, 2017).

Model derivation and parametrization

We model the expression dynamics of the TS by describing the change in time of the concentration of the [LacI] and [TetR] as a balance between their regulated production and degradation. In addition, we made the assumptions that the dynamics of the transcripts and promoter binding/unbinding is faster than the dynamics production and degradation of the repressor proteins, and that the reporters follow the same dynamics as their associated repressors.

The expression of LacI is regulated by TetR, which can inhibit the production of LacI by binding to the TetO promoter. Modelling this interaction as a repressive Hill function we can describe the evolution in time of LacI as, (1)

$$\frac{d[LacI]}{dt} = \frac{\beta_Y}{1 + (K_{TetR}[TetR])^{n_{TetR}}} - \delta_Y[LacI]$$

Where β_Y is the maximum production of LacI in the absence of the repressor TetR, K_{TetR} the TetR concentration producing half repression, n_{TetR} the Hill coefficient and δ_Y its degradation rate.

On the other hand, the expression of TetR is regulated at the same time by the repression of free LacI in the system [$LacI_f$] and the activation by AHL through the LuxR-AHL complex. Since the presence of free [$LacI_f$] is enough to silence the expression of [TetR] even in the presence of AHL, the production can be modelled as the product of two Hill functions,

(2)

$$\frac{d[TetR]}{dt} = \frac{\beta_X}{1 + (K_{LacI}[LacI_f])^{n_{LacI}}} \frac{(K_{AHL}[AHL])^{n_{AHL}}}{1 + (K_{AHL}[AHL])^{n_{AHL}}} - \delta_X[TetR]$$

Where β_X is the production rate in absence of LacI and saturating amounts of AHL. The amount of free LacI ([$LacI_f$]), is controlled by IPTG, which can bind free LacI impeding the binding with the LuxLac promoter,

(3)

$$[LacI_f] = \frac{[LacI]}{1 + K_{IPTG}[IPTG]}$$

In order to parametrize the mathematical model Eqs. (1-3), we compared the experimentally observed cellular states with the stable steady states of the theoretical dynamical system for different sets of concentrations of AHL and IPTG. The experimental steady states were obtained by using the gated expression in cellular populations (see Flow Cytometry for details). For each gated population, the state was accepted when it contained at least 15% of the cellular population.

The stable states for the mathematical model $([LacI]^*, [TetR]^*)$ were computed by solving Eqs. (1-3) at equilibrium condition $\frac{\mathrm{d}[LacI]}{\mathrm{d}t} = \frac{\mathrm{d}[TetR]}{\mathrm{d}t} = 0$,

$$[LacI]^* = f_1([TetR]^*) = \frac{\beta_Y/\delta_Y}{1 + (K_{TetR}[TetR]^*)^{n_{TetR}}}$$

$$[TetR]^* = f_2([LacI]^*; [IPTG], [AHL]) = \frac{\beta_X/\delta_X}{1 + \left(\frac{K_{LacI}[LacI]^*}{1 + K_{IPTG}[IPTG]}\right)^{n_{LacI}}} \frac{K_{AHL}[AHL]^{n_{AHL}}}{1 + (K_{AHL}[AHL])^{n_{AHL}}}$$

Thus, finding the available steady states for a given condition is reduced to finding the roots of $G(x)$ in the 1-dimensional equation $G([LacI]^*) = f_1\big(f_2([LacI]^*; [IPTG], [AHL])\big) - [LacI]^* = 0$. This was done by finding the number and approximate location of the roots by evaluating the sign of $G(x)$ over a logarithmically spaced set along the possible values of $[LacI]^* = \left[f_1\left(\frac{\beta_X}{\delta_X}\right), \frac{\beta_Y}{\delta_Y}\right]$. All the values found were refined by using the Brent-Dekker method with hyperbolic extrapolation. Finally, the stability of all the possible found states was addressed by evaluating the eigenvalues of the diagonalized Jacobian corresponding to Eqs (1-2).

In order to compare the computational steady states with fluorescence measurements we assumed a linear relationship between fluorescence and gene expression,

$$F_{RED} = \alpha_Y + \omega_Y[LacI]^*, \qquad F_{GREEN} = \alpha_X + \omega_X[TetR]^*$$

Thus, the parametrization of the problem is reduced to the inference of 11 identifiable parameters $\theta = \{\alpha_X, \alpha_Y, \tilde{\beta}_X, \tilde{\beta}_Y, K_{TetR}, K_{LacI}, , K_{AHL}, K_{IPTG}, n_{TetR}, n_{LacI}, n_{AHL}\}$, where $\tilde{\beta}_X$ and $\tilde{\beta}_Y$ summarize the parameter products $\tilde{\beta}_X = \omega_X\beta_X/\delta_X$, and $\tilde{\beta}_Y = \omega_Y\beta_Y/\delta_Y$

The ensemble of parameters in the mathematical model compatible with experimental observations was inferred using Markov Chain Monte Carlo. In particular, we made use of Multiple-try Differential Evolution Adaptative Metropolis algorithm (Laloy and Vrugt, 2012) using the PyDream implementation (Shockley et al., 2018). The Likelihood function used to evaluate the goodness of a given set of parameters is defined as,

$$\mathcal{L}(\theta|\text{data}) = \sum_{i=1}^{N} p_i \left(\min_{\text{j}} \left[\left(\frac{F^i_{RED\,exp} - F^{i,j}_{RED_{theo}}}{\sigma^i_{RED}} \right)^2 + \left(\frac{F^i_{GREEN\,exp} - F^{i,j}_{GREEN_{theo}}}{\sigma^i_{GREEN}} \right)^2 \right] \right)$$

Where the index i in the sum runs over all the experimentally detected cell states for each experimental condition. The experimental fluorescence $(F^i_{RED\,exp}, F^i_{GREEN\,exp})$, corresponds with the median of the gated population of cells for the *i*-th observed state. Similarly, $\sigma^i_{RED_{exp}}$ and $\sigma^i_{GREEN_{exp}}$ are the standard deviation of the gated populations of each state. The theoretical prediction for each parameter set θ and conditions

of state i, is given by $F^{i,j}_{RED_{theo}}$ and $F^{i,j}_{GREEN_{theo}}$, where the superindex j presents the different theoretically predicted stable states in the case of bistability. Finally, parameter p_i penalizes that for the condition given by state i (concentrations of AHL and IPTG) the number of different states detected experimentally is not the same than the number of stable states predicted in the mathematical model. Thus, p_i promotes parameter sets that match monostable and bistable regions between experimental and computational steady states. In particular $p_i = 0$ if the number of stable steady states match, and $p_i < 0$ otherwise. For the inference used in the manuscript, a value of $p_i = 10^3$ was used. The inferred parameters are given in Table 1.

Parameter	Median	Credibility Interval
α_X	364 a.u.	(252, 444) a.u.
α_Y	310 a.u.	(153, 422) a.u.
$\tilde{\beta}_X$	362 a.u.	(200, 598) a.u.
$\tilde{\beta}_Y$	438 a.u.	(322, 644) a.u.
K_{IPTG}	2.22 mM^{-1}	(1.04, 3.16) mM^{-1}
K_{AHL}	133 $\mu\mathrm{M}^{-1}$	(59.5, 318) $\mu\mathrm{M}^{-1}$
K_{LacI}	4.17 10^{-2} a.u.	(2.11, 8.90) 10^{-2} a.u.
K_{TetR}	27.4 10^{-2} a.u.	(6.12, 99.3) 10^{-2} a.u.
n_{LacI}	2.17	(1.00, 3.73)
n_{AHL}	1.61	(1.04,2.23)
n_{TetR}	2.29	(1.16, 5.01)

Table 1: **Parameters**. Summary of values of parameters inferred from the experimental data corresponding to the distributions of Figure 3. For each parameter, the median and the 95% credibility interval of each marginal distribution are indicated. The median of each parameter corresponds with the value used in the mathematical model for the rest of simulations of the manuscript.

Morphogen diffusion

The diffusion of the morphogens (AHL, IPTG, and aTc) on the agar plate is assumed to be a 2-D free diffusion determining the concentration of each chemical $\rho(x, y, t)$ at different positions of the plate. This is modelled through the partial differential equations

$$\frac{\partial \rho_{AHL}}{\partial t} = D\left(\frac{\partial^2 \rho_{AHL}}{\partial x^2} + \frac{\partial^2 \rho_{AHL}}{\partial y^2}\right),$$

$$\frac{\partial \rho_{IPTG}}{\partial t} = D\left(\frac{\partial^2 \rho_{IPTG}}{\partial x^2} + \frac{\partial^2 \rho_{IPTG}}{\partial y^2}\right).$$

This equation was solved by discretizing the space using the square experimental grid. The boundary conditions imposed by the experiment are given by the constant concentration of morphogen along one side of the square $\rho(0,y,t) = \rho_0$, and assuming sinks in the rest of the perimeter of the square$\rho(L,y,t) = \rho(x,0,t) = \rho(x,L,t) = 0$, where L is the length of the side of the square. In order to take into account the dilution effect of the initial concentration pipetted c_0 on the agar before stablishing the gradient, we set $\rho_0 = c_0\xi$. Parameters used for the grid assays are $\xi = 10^{-2}$ and $D = 2.5\ 10^{-3}\mathrm{cm}^2/\mathrm{h}$ (Basu et al., 2005, Miyamoto et al., 2018). Finally, in order to provide a time scale to the dynamics of protein, not available from the MCMC fitting of the steady states of the system, the degradation rate of the LacI and TetR was set to $\delta = 8.3\ \mathrm{h}^{-1}$((Wu et al., 2011).

Boundary position in the grid model was computed by analyzing the red fluorescence levels along the central strip of the grid $TeTR\left(x,\frac{L}{2},t\right)$. For each time point, a boundary was considered when the difference in fluorescence at both sides of the gradient was above a certain threshold $\left|TeTR\left(\frac{\ell}{2},\frac{L}{2},t\right) - TeTR\left(L-\frac{\ell}{2},\frac{L}{2},t\right)\right| > 250$, where ℓ is the distance between two adjacent cells of the grid. The position of the boundary x_b was set as the last cell of the grid were the concentration is above the mean point of the fluorescence range for each given timepoint $\left(TeTR\left(\frac{\ell}{2},\frac{L}{2},t\right) + TeTR\left(L-\frac{\ell}{2},\frac{L}{2},t\right)\right)/2$.

Acknowledgments

We thank Florence Gauye for excellent technical assistance and all Schaerli lab members for useful discussions. This work was funded by Swiss National Science Foundation Grant 31003A_175608 and an IPhD SystemsX.ch grant. RP-C acknowledges UCL Mathematics Clifford Fellowship.

Author Contributions

IB, RPC and YS designed research. IB performed experiments and analyzed data. RPC carried out the mathematical modelling and the data fitting. IB, RPC and YS wrote the manuscript. All authors have given approval to the final version of the manuscript.

Declaration of Interest

The authors declare no conflict of interest.

References

ALON, U. 2007. Network motifs: theory and experimental approaches. *Nature Reviews Genetics,* 8**,** 450-61.

ANDREWS, L. B., NIELSEN, A. A. K. & VOIGT, C. A. 2018. Cellular checkpoint control using programmable sequential logic. *Science,* 361**,** eaap8987.

AXELROD, K., SANCHEZ, A. & GORE, J. 2015. Phenotypic states become increasingly sensitive to perturbations near a bifurcation in a synthetic gene network. *Elife,* 4**,** e07935.

BALASKAS, N., RIBEIRO, A., PANOVSKA, J., DESSAUD, E., SASAI, N., PAGE, K. M., BRISCOE, J. & RIBES, V. 2012. Gene regulatory logic for reading the Sonic Hedgehog signaling gradient in the vertebrate neural tube. *Cell,* 148**,** 273-84.

BASHOR, C. J. & COLLINS, J. J. 2018. Understanding Biological Regulation Through Synthetic Biology. *Annual Review of Biophysics, Vol 47,* 47**,** 399-423.

BASU, S., GERCHMAN, Y., COLLINS, C. H., ARNOLD, F. H. & WEISS, R. 2005. A synthetic multicellular system for programmed pattern formation. *Nature,* 434**,** 1130-4.

BEAL, J., NGUYEN, T., GOROCHOWSKI, T. E., GONI-MORENO, A., SCOTT-BROWN, J., MCLAUGHLIN, J. A., MADSEN, C., ALERITSCH, B., BARTLEY, B., BHAKTA, S., BISSELL, M., HAIR, S. C., CLANCY, K., LUNA, A., LE NOVERE, N., PALCHICK, Z., POCOCK, M., SAURO, H., SEXTON, J. T., TABOR, J. J., VOIGT, C. A., ZUNDEL, Z., MYERS, C. & WIPAT, A. 2019. Communicating Structure and Function in Synthetic Biology Diagrams. *Acs Synthetic Biology,* 8**,** 1818-1825.

BOEHM, C. R., GRANT, P. K. & HASELOFF, J. 2018. Programmed hierarchical patterning of bacterial populations. *Nat Commun,* 9**,** 776.

BRISCOE, J. & SMALL, S. 2015. Morphogen rules: design principles of gradient-mediated embryo patterning. *Development,* 142**,** 3996-4009.

BROPHY, J. A. & VOIGT, C. A. 2014. Principles of genetic circuit design. *Nat Methods,* 11**,** 508-20.

CAMERON, D. E., BASHOR, C. J. & COLLINS, J. J. 2014. A brief history of synthetic biology. *Nat Rev Microbiol,* 12**,** 381-90.

CAO, Y., FENG, Y., RYSER, M. D., ZHU, K., HERSCHLAG, G., CAO, C., MARUSAK, K., ZAUSCHER, S. & YOU, L. 2017. Programmable assembly of pressure sensors using pattern-forming bacteria. *Nat Biotechnol,* 35**,** 1087-1093.

CHEN, D. & ARKIN, A. P. 2012. Sequestration-based bistability enables tuning of the switching boundaries and design of a latch. *Molecular Systems Biology,* 8**,** 620.

CLARK, E. 2017. Dynamic patterning by the Drosophila pair-rule network reconciles long-germ and short-germ segmentation. *PLoS Biol,* 15**,** e2002439.

COHEN, M., KICHEVA, A., RIBEIRO, A., BLASSBERG, R., PAGE, K. M., BARNES, C. P. & BRISCOE, J. 2015. Ptch1 and Gli regulate Shh signalling dynamics via multiple mechanisms. *Nat Commun,* 6**,** 6709.

COHEN, M., PAGE, K. M., PEREZ-CARRASCO, R., BARNES, C. P. & BRISCOE, J. 2014. A theoretical framework for the regulation of Shh morphogen-controlled gene expression. *Development,* 141**,** 3868-3878.

DAVIES, J. 2017. Using synthetic biology to explore principles of development. *Development,* 144**,** 1146-1158.

DAVIES, J. A. & CACHAT, E. 2016. Synthetic biology meets tissue engineering. *Biochem Soc Trans,* 44**,** 696-701.

DHARMARAJAN, L., KALTENBACH, H. M., RUDOLF, F. & STELLING, J. 2019. A Simple and Flexible Computational Framework for Inferring Sources of Heterogeneity from Single-Cell Dynamics. *Cell Syst,* 8**,** 15-26.e11.

DIFRISCO, J. & JAEGER, J. 2019. Beyond networks: mechanism and process in evo-devo. *Biology & Philosophy,* 34**,** 54.

EBRAHIMKHANI, M. R. & EBISUYA, M. 2019. Synthetic developmental biology: build and control multicellular systems. *Curr Opin Chem Biol,* 52**,** 9-15.

ELOWITZ, M. B. & LEIBLER, S. 2000. A synthetic oscillatory network of transcriptional regulators. *Nature,* 403**,** 335-8.

FERRELL, J. E. 2002. Self-perpetuating states in signal transduction: positive feedback, double-negative feedback and bistability. *Current Opinion in Cell Biology,* 14**,** 140-148.

GAO, X. J., CHONG, L. S., KIM, M. S. & ELOWITZ, M. B. 2018. Programmable protein circuits in living cells. *Science,* 361**,** 1252-1258.

GARDNER, T. S., CANTOR, C. R. & COLLINS, J. J. 2000. Construction of a genetic toggle switch in Escherichia coli. *Nature,* 403**,** 339-42.

GILBERT, C. & ELLIS, T. 2018. Biological Engineered Living Materials: Growing Functional Materials with Genetically Programmable Properties. *ACS Synthetic Biology,* 8**,** 1-15.

GRANT, P. K., DALCHAU, N., BROWN, J. R., FEDERICI, F., RUDGE, T. J., YORDANOV, B., PATANGE, O., PHILLIPS, A. & HASELOFF, J. 2016. Orthogonal intercellular signaling for programmed spatial behavior. *Mol Syst Biol,* 12**,** 849.

GREEN, J. B. & SHARPE, J. 2015. Positional information and reaction-diffusion: two big ideas in developmental biology combine. *Development,* 142**,** 1203-11.

GUANTES, R. & POYATOS, J. F. 2008. Multistable Decision Switches for Flexible Control of Epigenetic Differentiation. *PLoS Comput Biol,* 4**,** e1000235.

HEALY, C. P. & DEANS, T. L. 2019. Genetic circuits to engineer tissues with alternative functions. *J Biol Eng,* 13**,** 39.

ISALAN, M., LEMERLE, C. & SERRANO, L. 2005. Engineering gene networks to emulate Drosophila embryonic pattern formation. *Plos Biology,* 3**,** 488-496.

JUNKER, J. P., PETERSON, K. A., NISHI, Y., MAO, J. H., MCMAHON, A. P. & VAN OUDENAARDEN, A. 2014. A Predictive Model of Bifunctional Transcription Factor Signaling during Embryonic Tissue Patterning. *Developmental Cell,* 31**,** 448-460.

KITADA, T., DIANDRETH, B., TEAGUE, B. & WEISS, R. 2018. Programming gene and engineered-cell therapies with synthetic biology. *Science,* 359**,** eaad1067.

KOGENARU, M. & TANS, S. J. 2014. An improved Escherichia coli strain to host gene regulatory networks involving both the AraC and LacI inducible transcription factors. 8**,** 2.

KRAUT, R. & LEVINE, M. 1991. Mutually Repressive Interactions between the Gap Genes Giant and Kruppel Define Middle Body Regions of the Drosophila Embryo. *Development,* 111**,** 611-621.

LALOY, E. & VRUGT, J. A. 2012. High-dimensional posterior exploration of hydrologic models using multiple-try DREAM((ZS)) and high-performance computing. *Water Resources Research,* 48**,** W01526.

LEBAR, T., BEZELJAK, U., GOLOB, A., JERALA, M., KADUNC, L., PIRŠ, B., STRAŽAR, M., VUČKO, D., ZUPANČIČ, U., BENČINA, M., FORSTNERIČ, V., GABER, R., LONZARIĆ, J., MAJERLE, A., OBLAK, A., SMOLE, A. & JERALA, R. 2014. A bistable genetic switch based on designable DNA-binding domains. *Nat Commun,* 5**,** 5007.

LI, P., MARKSON, J. S., WANG, S., CHEN, S., VACHHARAJANI, V. & ELOWITZ, M. B. 2018. Morphogen gradient reconstitution reveals Hedgehog pathway design principles. *Science,* 360**,** 543-548.

LITCOFSKY, K. D., AFEYAN, R. B., KROM, R. J., KHALIL, A. S. & COLLINS, J. J. 2012. Iterative plug-and-play methodology for constructing and modifying synthetic gene networks. *Nat Methods,* 9**,** 1077-80.

LOPES, F. J. P., VIEIRA, F. M. C., HOLLOWAY, D. M., BISCH, P. M. & SPIROV, A. V. 2008a. Spatial Bistability Generates hunchback Expression Sharpness in the Drosophila Embryo. *PLoS Comput Biol,* 4**,** e1000184.

LOPES, F. J. P., VIEIRA, F. M. C., HOLLOWAY, D. M., BISCH, P. M. & SPIROV, A. V. 2008b. Spatial Bistability Generates hunchback Expression Sharpness in the Drosophila Embryo. *Plos Computational Biology,* 4.

LOU, C. B., LIU, X. L., NI, M., HUANG, Y. Q., HUANG, Q. S., HUANG, L. W., JIANG, L. L., LU, D., WANG, M. C., LIU, C., CHEN, D. Z., CHEN, C. Y., CHEN, X. Y., YANG, L., MA, H. S., CHEN, J. G. & OUYANG, Q. 2010. Synthesizing a novel genetic sequential logic circuit: a push-on push-off switch. *Molecular Systems Biology,* 6**,** 350.

LUGAGNE, J. B., SOSA CARRILLO, S., KIRCH, M., KOHLER, A., BATT, G. & HERSEN, P. 2017. Balancing a genetic toggle switch by real-time feedback control and periodic forcing. *Nat Commun,* 8**,** 1671.

LUO, N., WANG, S. & YOU, L. 2019. Synthetic Pattern Formation. *Biochemistry,* 58**,** 1478-1483.

MIYAMOTO, S., ATSUYAMA, K., EKINO, K. & SHIN, T. 2018. Estimating the Diffusion Coefficients of Sugars Using Diffusion Experiments in Agar-Gel and Computer Simulations. *Chem Pharm Bull (Tokyo),* 66**,** 632-636.

MOSER, F., THAM, E., GONZALEZ, L. M., LU, T. K. & VOIGT, C. A. 2019. Light-Controlled, High-Resolution Patterning of Living Engineered Bacteria Onto Textiles, Ceramics, and Plastic. *Advanced Functional Materials,* 29.

NARULA, J., WILLIAMS, C. J., TIWARI, A., MARKS-BLUTH, J., PIMANDA, J. E. & IGOSHIN, O. A. 2013. Mathematical model of a gene regulatory network reconciles effects of genetic perturbations on hematopoietic stem cell emergence. *Developmental Biology,* 379**,** 258-269.

NGUYEN, P. Q., COURCHESNE, N. D., DURAJ-THATTE, A., PRAVESCHOTINUNT, P. & JOSHI, N. S. 2018. Engineered Living Materials: Prospects and Challenges for Using Biological Systems to Direct the Assembly of Smart Materials. *Adv Mater,* 30**,** e1704847.

NIELSEN, J. & KEASLING, J. D. 2016. Engineering Cellular Metabolism. *Cell,* 164**,** 1185-1197.

NIKOLAEV, E. V. & SONTAG, E. D. 2016. Quorum-Sensing Synchronization of Synthetic Toggle Switches: A Design Based on Monotone Dynamical Systems Theory. *PLoS Comput Biol,* 12**,** e1004881.

PADIRAC, A., FUJII, T. & RONDELEZ, Y. 2012. Bottom-up construction of in vitro switchable memories. *Proc Natl Acad Sci U S A,* 109**,** E3212-20.

PANOVSKA-GRIFFITHS, J., PAGE, K. M. & BRISCOE, J. 2013. A gene regulatory motif that generates oscillatory or multiway switch outputs. *J R Soc Interface,* 10**,** 20120826.

PEREZ-CARRASCO, R., BARNES, C. P., SCHAERLI, Y., ISALAN, M., BRISCOE, J. & PAGE, K. M. 2018. Combining a Toggle Switch and a Repressilator within the AC-DC Circuit Generates Distinct Dynamical Behaviors. *Cell Syst,* 6**,** 521-530 e3.

PEREZ-CARRASCO, R., GUERRERO, P., BRISCOE, J. & PAGE, K. M. 2016. Intrinsic Noise Profoundly Alters the Dynamics and Steady State of Morphogen-Controlled Bistable Genetic Switches. *PLoS Comput Biol,* 12**,** e1005154.

POTVIN-TROTTIER, L., LORD, N. D., VINNICOMBE, G. & PAULSSON, J. 2016. Synchronous long-term oscillations in a synthetic gene circuit. *Nature,* 538**,** 514-517.

PURCELL, O. & LU, T. K. 2014. Synthetic analog and digital circuits for cellular computation and memory. *Curr Opin Biotechnol,* 29**,** 146-55.

R CORE TEAM 2017. R: A language and environment for statistical computing. R Foundation for Statistical Computing. *Vienna, Austria*.

ROGERS, K. W. & SCHIER, A. F. 2011. Morphogen Gradients: From Generation to Interpretation. *Annual Review of Cell and Developmental Biology, Vol 27,* 27**,** 377-407.

SAGNER, A. & BRISCOE, J. 2017. Morphogen interpretation: concentration, time, competence, and signaling dynamics. *Wiley Interdiscip Rev Dev Biol,* 6**,** e271.

SAKA, Y. & SMITH, J. C. 2007. A mechanism for the sharp transition of morphogen gradient interpretation in Xenopus. *Bmc Developmental Biology,* 7**,** 47.

SANTOS-MORENO, J. & SCHAERLI, Y. 2019a. Multistable and dynamic CRISPRi-based synthetic circuits in E. coli. *bioRxiv***,** 756338.

SANTOS-MORENO, J. & SCHAERLI, Y. 2019b. Using Synthetic Biology to Engineer Spatial Patterns. *Advanced Biosystems,* 3**,** 1800280.

SCHAERLI, Y., MUNTEANU, A., GILI, M., COTTERELL, J., SHARPE, J. & ISALAN, M. 2014. A unified design space of synthetic stripe-forming networks. *Nat Commun,* 5**,** 4905.

SCHINDELIN, J., ARGANDA-CARRERAS, I., FRISE, E., KAYNIG, V., LONGAIR, M., PIETZSCH, T., PREIBISCH, S., RUEDEN, C., SAALFELD, S., SCHMID, B., TINEVEZ, J.-Y., WHITE, D. J., HARTENSTEIN, V., ELICEIRI, K., TOMANCAK, P. & CARDONA, A. 2012. Fiji: an open-source platform for biological-image analysis. *Nature Methods,* 9**,** 676-682.

SEKINE, R., YAMAMURA, M., AYUKAWA, S., ISHIMATSU, K., AKAMA, S., TAKINOUE, M., HAGIYA, M. & KIGA, D. 2011. Tunable synthetic phenotypic diversification on Waddington's landscape through autonomous signaling. *Proc Natl Acad Sci U S A,* 108**,** 17969-73.

SHOCKLEY, E. M., VRUGT, J. A. & LOPEZ, C. F. 2018. PyDREAM: high-dimensional parameter inference for biological models in python. *Bioinformatics,* 34**,** 695-697.

SOKOLOWSKI, T. R., ERDMANN, T. & TEN WOLDE, P. R. 2012. Mutual Repression Enhances the Steepness and Precision of Gene Expression Boundaries. *PLoS Comput Biol,* 8**,** e1002654.

SRINIVASAN, S., HU, J. S., CURRLE, D. S., FUNG, E. S., HAYES, W. B., LANDER, A. D. & MONUKI, E. S. 2014. A BMP-FGF morphogen toggle switch drives the ultrasensitive expression of multiple genes in the developing forebrain. *PLoS Comput Biol,* 10**,** e1003463.

VERD, B., CROMBACH, A. & JAEGER, J. 2014. Classification of transient behaviours in a time-dependent toggle switch model. *BMC Syst Biol,* 8**,** 43

VERD, B., MONK, N. A. M. & JAEGER, J. 2019. Modularity, criticality, and evolvability of a developmental gene regulatory network. *Elife,* 8**,** e42832.

WANG, L., WALKER, B. L., IANNACCONE, S., BHATT, D., KENNEDY, P. J. & TSE, W. T. 2009. Bistable switches control memory and plasticity in cellular differentiation. *Proceedings of the National Academy of Sciences of the United States of America,* 106**,** 6638-6643.

WEBER, M. & BUCETA, J. 2013. Stochastic stabilization of phenotypic States: the genetic bistable switch as a case study. *PLoS One,* 8**,** e73487.

WEBSTER, V. A., CHAPIN, K. J., HAWLEY, E. L., PATEL, J. M., AKKUS, O., CHIEL, H. J. & QUINN, R. D. 2016. Aplysia Californica as a Novel Source of Material for Biohybrid Robots and Organic Machines. *Biomimetic and Biohybrid Systems, Living Machines 2016,* 9793**,** 365-374.

WOLPERT, L. 1996. One hundred years of positional information. *Trends in Genetics,* 12**,** 359-364.

WU, C.-H., LEE, H.-C. & CHEN, B.-S. 2011. Robust synthetic gene network design via library-based search method. *Bioinformatics,* 27**,** 2700-2706.

WU, M., SU, R. Q., LI, X., ELLIS, T., LAI, Y. C. & WANG, X. 2013. Engineering of regulated stochastic cell fate determination. *Proc Natl Acad Sci U S A,* 110**,** 10610-5.

XIE, M. Q. & FUSSENEGGER, M. 2018. Designing cell function: assembly of synthetic gene circuits for cell biology applications. *Nature Reviews Molecular Cell Biology,* 19**,** 507-525.

YANG, Y., NEMHAUSER, J. L. & KLAVINS, E. 2019. Synthetic Bistability and Differentiation in Yeast. *ACS Synthetic Biology,* 8**,** 929-936.

ZAGORSKI, M., TABATA, Y., BRANDENBERG, N., LUTOLF, M. P., TKACIK, G., BOLLENBACH, T., BRISCOE, J. & KICHEVA, A. 2017. Decoding of position in the developing neural tube from antiparallel morphogen gradients. *Science,* 356**,** 1379-1383.

ZHANG, L., RADTKE, K., ZHENG, L., CAI, A. Q., SCHILLING, T. F. & NIE, Q. 2012. Noise drives sharpening of gene expression boundaries in the zebrafish hindbrain. *Molecular Systems Biology,* 8**,** 613.

ZHAO, C., BIN, A., YE, W. M., FAN, Y. & DI, Z. R. 2015. Motif for controllable toggle switch in gene regulatory networks. *Physica a-Statistical Mechanics and Its Applications,* 419**,** 498-505.